Environ Fluid Mech
DOI 10.1007/s10652-016-9476-x

ORIGINAL ARTICLE

Characterization of bedload intermittency near the threshold of motion using a Lagrangian sediment transport model

Christian González[1] · David H. Richter[2] · Diogo Bolster[2] · Samuel Bateman[3] · Joseph Calantoni[3] · Cristián Escauriaza[1]

Received: 16 September 2015 / Accepted: 21 July 2016

Abstract At the smallest scales of sediment transport in rivers, the coherent structures of the turbulent boundary layer constitute the fundamental mechanisms of bedload transport, locally increasing the instantaneous hydrodynamic forces acting on sediment particles, and mobilizing them downstream. Near the critical threshold for initiating sediment motion, the interactions of the particles with these unsteady coherent structures and with other sediment grains, produce localized transport events with brief episodes of collective motion occurring due to the near-bed velocity fluctuations. Simulations of these flows pose a significant challenge for numerical models aimed at capturing the physical processes and complex non-linear interactions that generate highly intermittent and self-similar bedload transport fluxes. In this investigation we carry out direct numerical simulations of the flow in a rectangular flat-bed channel, at a Reynolds number equal to $Re = 3632$, coupled with the discrete element method to simulate the dynamics of spherical particles near the bed. We perform two-way coupled Lagrangian simulations of 48,510 sediment particles, with 4851 fixed particles to account for bed roughness. Our simulations consider a total of eight different values of the non-dimensional Shields parameter to study the evolution of transport statistics. From the trajectory and velocity of each sediment particle, we compute the changes in the probability distribution functions of velocities, bed activity, and jump lengths as the Shields number increases. For the lower shear stresses, the intermittency of the global bedload transport flux is described by computing the singularity or multifr actal spectrum of transport, which also characterizes the widespread range of transport event magnitudes. These findings can help to identify the mechanisms of sediment transport at

✉ Cristián Escauriaza
cescauri@ing.puc.cl

[1] Departamento de Ingeniería Hidráulica y Ambiental, Pontificia Universidad Católica de Chile, Santiago, Chile

[2] Department of Civil and Environmental Engineering and Earth Sciences, University of Notre Dame, Notre Dame, USA

[3] Marine Geosciences Division, Stennis Space Center, Naval Research Laboratory, Clarksdale, MS, USA

Published online: 05 August 2016

the particle scale. The statistical analysis can also be used as an ingredient to develop larger, upscaled models for predicting mean transport rates, considering the variability of entrainment and deposition that characterizes the transport near the threshold of motion.

Keywords Direct numerical simulations · Lagrangian particle model · Bedload transport · Discrete element method · Intermittency

List of symbols

C	Volumetric concentration of particles
C_D	Drag coefficient
d	Particles diameter
D_0	Fractal, Hausdorff or box-counting dimension of the bedload flux
d^+	Non-dimensional diameter
e	Coefficient of restitution
F^{col}	Force due to inter-particles collisions
F_i	Feedback force from the particles to the flow
Fr	Froude number
f_i	External pressure gradient applied to the flow
$f^p_{i,\eta}$	Hydrodynamic drag force felt by a particle
$f(\alpha)$	Singularity spectrum
g	Gravity acceleration
h	Length scale of a domain
k	Shape parameter of the Gamma distribution function
$M(q, r\Delta t)$	q-th Order statistical moment of μ_i
$N(r\Delta t)$	Number of time windows of size $r\Delta t$ contained in the total time when transport occurs
P	Pressure field of the flow
Re	Reynolds number based on bulk velocity
Re_p	Particle Reynolds number based on the particle velocity relative to the flow
Re^*_p	Particle Reynolds number based on the friction velocity
Re_τ	Friction Reynolds number
r	Integer for computing different sampling time scale of sediment transport
$r^+_{inactive}$	Dimensionless radius of the inactive particles
$S(t)$	Cumulative amount of particles that have crossed the control plane until time t
St_k	Stokes number
$s(t)$	Number of particles crossing the control plane in a given time step Δt
T_{max}	Total time of simulation
$T(r\Delta t)$	Total width of periods with no transport that are larger than $r\Delta t$
t	Time
U	Bulk velocity of the flow
u_{f_i}	Velocity of the fluid at the particle location ($i = 1, 2, 3$)
u_j	Instantaneous velocity components of the flow ($j = 1, 2, 3$)
u_p	Particles velocity in the streamwise direction
u^+	Dimensionless bulk velocity
u^*	Friction velocity
v_{cr}	Arbitrary critical velocity which delineate active motions
v_p	Particles velocity in the spanwise direction
v_{p_i}	Instantaneous particle velocity component ($i = 1, 2, 3$)

w_p	Particles velocity in the vertical direction
w_η^j	Linear geometric weight for the projection of the feedback forces from particles to flow
x_i	Cartesian coordinates ($i = 1, 2, 3$). Also written as x, y, z
x_L	Streamwise dimension of the channel
Y	Young's modulus
y_L	Spanwise dimension of the channel
z_L	Vertical dimension of the channel
z^+	Dimensionless vertical coordinate
α	Hölder exponent
β	Scale parameter of the Gamma distribution function
Δt	Time step used by the flow solver
Δt_p	Time step used by the particles solver
ΔV_η	Volume of a computational cell
δ	Boundary layer thickness
ζ	Scaling exponent function
θ	Shields parameter
ϑ	Poisson's ratio
κ	von Kármán constant
λ	Distance traveled downstream by the particles
μ_f	Coefficient of friction
μ_i	Mass fraction of sediment that cross the reference plane between two successive plateaus
ν	Kinematic viscosity of the fluid
ρ_f	Density of the fluid
ρ_p	Density of the particles
τ_0	Bed shear stress
$\mathcal{X}$	Random variable distributing Gamma
$\forall_p$	Volume of a particle

1 Introduction

The initiation of motion and sediment transport processes near the bed play an important role across a wide range of temporal and spatial scales in fluvial systems. These phenomena include the dynamics and interactions of particles, bedform generation, and larger scale processes such as bed resistance, changes of the flow hydrodynamics and impacts on the entire morphodynamics of the river. The collective dynamics of sediment particles displays a complex behavior that is to date not fully understood, as it is mostly dominated by complex nonlinear interactions of the sediment grains with the turbulent boundary layer, and with other particles in motion or lying on the bed. The identification of the fundamental mechanisms that control bedload transport in rivers and the prediction of sediment dynamics at the particle scale still present significant challenges for computational models and experimental investigations, and continue to be the subject of extensive research [24, 44, 45].

At conditions near the threshold of motion, a distinctive feature of bedload transport is the intermittency of the sediment flux, characterized by frequent and localized transport

events in which groups of particles are displaced by saltating, rolling or sliding on the bed [20, 21, 27]. From the early pioneering work of Einstein [21], the estimation of the sediment flux has been formulated in many cases using a probabilistic approach, representing the sediment jump lengths and other aspects of the particle dynamics using probability distribution functions. Recent investigations, however, have shown that the intermittent fluxes produced at low transport stages yield a non-Gaussian behavior, with thick tails of the probability distribution functions due to frequent extreme events and long correlations, violating critical assumptions required for Gaussian/Fickian transport [e.g., 4, 23, 35, 41, 46].

This characteristic anomalous scaling of the sediment flux [41] is induced by the near-bed coherent structures of the turbulent boundary layer that interact with the grains. The coherent turbulent motions produce well-known sweeps, ejections, inward and outward interactions of flow velocity fluctuations, among other complex hydrodynamic features that can increase the instantaneous forces acting on sediment grains [see 1, 2, 36, for details]. The bedload flux is therefore closely related to the interactions between these coherent structures of the boundary layer and the sediment particles.

Previous investigations have demonstrated that sweeps are strongly correlated to entrainment events [29–31]. Outward interactions have also been recognized as major mechanisms for entrainment [9, 37, 40]. Thus, positive fluctuations in the streamwise velocity contribute to particle motion. Although under certain conditions, ejections could play a more relevant role than outward interactions [42], e.g. when sediment is poorly sorted [55]. In addition to the instantaneous hydrodynamic forces that act on sediment particles produced by the near-bed coherent structures, intermittency can also arise due to the bed configuration, as particles can rest in positions less exposed to the flow or "protective pockets" that are formed by other surrounding particles. Particles at rest thus impose an additional restriction to the movement, favoring the intermittency of the transport flux.

Models aimed at understanding the intermittency of bedload transport and the initiation of motion processes need to capture the turbulent events on the bed, the space-time variability of the hydrodynamic forces, and the interactions and collisions between particles. Recent advances in Lagrangian particle models of sediment transport have reproduced many features of the bedload flux under different hydrodynamic conditions, representing the sediment particles as spheres with the discrete-element method (DEM) [15]. Simulations have been performed either with the one-way coupling approach in dilute flows, in which the flow is not affected by the particle dynamics, or two-way coupling when particles can alter the dynamics of the flow [7]. Some current models are listed below, where different approaches and assumptions are considered.

Chang and Scotti [17] initially performed simulations of sediment grains in a channel with a rigid wavy bottom to recreate a fixed ripple on the bed. They used a one-way coupling approach with Large-Eddy Simulations (LES) to solve the flow, imposing periodic boundary conditions in the streamwise and spanwise directions. Their setup was characterized by a Reynolds number $Re = 3250$, simulating 14,000 particles with Stokes numbers ranging from 1×10^{-4} to 4×10^{-4}. Their work showed that the suspension of particles above the ripple was divided into two steps: i) a cloud of suspended grains appearing downstream from the top of the ripple and ii) ejection of particles into the water column occurring from this sediment cloud.

Escauriaza and Sotiropoulos [23] computed the flow and particle dynamics past a cylinder in a flat-bed channel using the Detached-Eddy Simulation (DES) approach. DES is a hybrid turbulence model that involves solving the Unsteady Reynolds-Averaged

Navier–Stokes equations (URANS) near solid walls, and LES in the rest of the domain. They carried out one-way coupling simulations of non-interacting particles that could only collide with the bed and the cylinder. In their simulations they considered up to 200,000 sediment grains initially placed on the bed upstream of the cylindrical obstacle, in a flow with a Reynolds number equal to Re = 39,000. This work showed for the first time the mechanisms of transport at the particle level that generate the intermittency of the sediment flux in conditions near the threshold of motion. The quasi-periodic dynamics of the turbulent horseshoe vortex system around the cylinder locally increased the hydrodynamic forces, producing seemingly random episodes of transport in which groups of particles were entrained, while near-bed vortices formed streaks of particles in low shear-stress regions. The intermittent cumulative bedload flux was calculated as the total number of particles that crossed a control plane downstream of the obstacle, which was described by the fractal curve known as the devil's staircase distribution [6]. The investigation of Escauriaza and Sotiropoulos [23] was also the first to characterize the intermittency in conditions near the threshold of motion, by computing the multifractal spectrum of bedload transport in the cumulative sediment transport series. Similar results were obtained by Link et al. [35], who also observed this multifractal behavior in a similar configuration, but in a non-flat scoured bed, showing how the statistics changed as the bed was eroded by the horseshoe vortex system.

Soldati and Marchioli [47] discussed the applicability of the point-particle approach in sediment transport simulations, comparing a flat-bed channel and a wavy channel through direct numerical simulation (DNS) and LES respectively. The flow they simulated had friction Reynolds numbers (Re_τ) ranging from 150 to 300, where sediment particles were modeled as non-interacting, spherical, and rigid elements. The friction Reynolds number is defined as $Re_\tau = u^* h/\nu$, where u^* is the friction velocity, h the length scale of the domain, and ν the kinematic viscosity. They focused on the development of different strategies that could be carried out on computational models to study sedimentation and resuspension processes.

Schmeeckle [45] combined LES for computing the flow with a DEM approach for solving the particle dynamics on a flat-bed channel with periodic boundary conditions in streamwise and spanwise directions. The sediment was represented by around 115,000 spherical elements in a flow with Re ranging from 8000 to 48,000. He employed a two-way coupling approach, including collisions among grains. The results of this model showed that in bedload transport the peak in the sediment flux occurs very near the top of the non-moving bed of grains, and that saltation played a secondary role as a mechanism of transport near the bed. The range of parameters explored in this work considered conditions well above the threshold of motion for the sediment grains, which produced continuous transport without intermittency on the bedload flux.

Dallali and Armenio [18] carried out one-way and two-way coupled simulations using LES in a flat bed channel with periodic boundary conditions. They represented the dispersed phase using a continuum Eulerian model instead of a Lagrangian particle model. Their cases of study were determined by a friction Reynolds number equal to $Re_\tau = 600$, and sediments with non-dimensional diameters $d^+ = 1, 3, 5$, and 6.5, where $d^+ = u^* d/\nu$, and d is the representative diameter of the sediment grains. This non-dimensional particle diameter is also known as particle Reynolds number (Re_p^*). All cases were above the Shields curve, i.e. over the threshold of motion. They found that the velocity and concentration profiles depended upon the nature of the coupling included in their model. This suggested that two-way coupling is needed to capture certain critical features of the flow,

for example, the sediment buoyancy contribution to the momentum transport, or the changes to the von Kármán constant of the velocity profile.

Vowinckel et al. [53] modeled a flat-bed channel with DNS, using the immersed boundary method (IBM) for the particles. Their simulations considered between 13,500 and 27,000 immobile particles fixed to the bed along with 0–13,500 mobile particles in a channel flow with $Re = 2941$ and a Shields parameters above and below the critical value for entrainment. Vowinckel et al. [53], in agreement with other studies such as Alletto and Breuer [3], recognized that a point-particle approach is suitable for representing sediment transport at these scales if grain collisions and feedbacks with the flow are considered. In this specific point they also agree with Schmeeckle [45], who demonstrated that the two-way coupling approach and sphere collisions are realistic assumptions, neglecting the mass coupling for stability reasons. It is worth mentioning that the values below the critical Shields number for sediment motion in [53] were used to study the influence of sediment in turbulence modulation, rather than the intermittency in transport.

As seen above, many studies have focused on the fluid-particle interaction using computational models, and while identified as important, the intermittent processes of transport generated near the threshold of motion have not been deeply explored or characterized. Following these previous works, we carry out simulations using DNS, coupled in a two-way manner to a DEM particle solver which computes collisions between grains using a point-particle approach. Here we present this model as a tool for gaining insights in the mechanisms that generate intermittency in sediment transport.

The paper is organized as follows: In Sect. 2 we present a brief description of the numerical methods we use to perform DNS and the coupling with the DEM particle model. In Sect. 3 we analyze the statistics of sediment transport based on the velocities and trajectories of particles, i.e. velocity histograms, activity, and jump lengths, also including a characterization of intermittency at low transport stages with the multifractal spectrum of the bedload flux. Finally, Sect. 4 contains the conclusions, the summary of the findings of our research, and some suggested possible future directions of study.

2 Methods

2.1 Carrier phase equations

The fluid phase is governed by the incompressible Navier–Stokes mass and momentum conservation equations:

$$\frac{\partial u_j}{\partial x_j} = 0, \tag{1}$$

$$\frac{\partial u_i}{\partial t} + u_j \frac{\partial u_i}{\partial x_j} = -\frac{1}{\rho_f}\frac{\partial P}{\partial x_i} + \nu \frac{\partial^2 u_i}{\partial x_j \partial x_j} + \frac{1}{\rho_f} F_i + \frac{f_i}{\rho_f}, \tag{2}$$

where x_i are the cartesian coordinates ($i = 1, 2, 3$) in the streamwise, spanwise and vertical directions respectively, u_j are the instantaneous velocity components of the fluid, P is the pressure, ρ_f is the density of the fluid, ν the kinematic viscosity, f_i is an additional force which represents an externally applied pressure gradient in the streamwise direction, and F_i is the feedback force from the particles that acts on the fluid. F_i is computed by linearly projecting and summing the drag force from all particles within a given computational cell:

$$F_i = -\sum_{\eta} \frac{w_{\eta}^{j}}{\Delta V_{\eta}} f_{i,\eta}^{p}, \tag{3}$$

where the summation is over all particles η in the grid cells, which share a computational node j. ΔV_{η} is the volume of the cell in which the particle resides, w_{η}^{j} is the linear geometric weight based on the distance from node j to the particle η and $f_{i,\eta}^{p}$ is the hydrodynamic drag force felt by particle η (second term on the right hand side of 4, below). Additional details can be found in the work of Richter and Sullivan [43].

2.2 Dispersed phase equations

The particle motion is governed by Newton's second law, written as follows [15]:

$$\rho_p \forall_p \frac{dv_{p_i}}{dt} = (\rho_p - \rho_f)\forall_p g_i + \frac{1}{2}\rho_f C_D A |u_{f_i} - v_{p_i}|(u_{f_i} - v_{p_i}) + F^{col}, \tag{4}$$

where ρ_p and $\forall_p$ are the density and volume of a spherical particle, v_{p_i} is the particle velocity in the i direction of the Cartesian frame, u_{f_i} is the velocity of the fluid at the particle location computed using a sixth-order Lagrange interpolation, F^{col} is the collision force due to other particles (see Appendix 1), and C_D is the drag coefficient, calculated from the following expression [12]:

$$C_D = \frac{24}{Re_p}(1 + 0.15 Re_p^{0.697}), \tag{5}$$

where $Re_p = d_p|v_{pi} - u_{fi}|/v$ is the particle Reynolds number based on the magnitude of the slip velocity $v_{pi} - u_{fi}$.

The first term on the right hand side of 4 corresponds to gravitational and buoyancy forces, and the last term refers to the hydrodynamic drag force. For simplicity we consider the drag force as the only interaction with the fluid, since it is typically much larger in magnitude than other forces such as added mass, lift, Basset, or pressure drag. For example, Basset forces have been derived for Stokes flows, where the inertia terms in the Navier–Stokes equations are negligible. Consequently, it should be expected that Basset forces will be negligible unless the particle Reynolds number is small, i.e. when $Re_s << 1$, where Re_s is the particle Reynolds number referred to the particles diameter and settling velocity [38, 39]. Throughout this work, we analyze flows where $Re_s \sim 6$–36. The low-Reynolds number simulations of Escauriaza and Sotiropoulos [22] in chaotically-advected flows, demonstrate that lift, added mass, pressure drag, and viscous stresses are at least one order of magnitude smaller than drag. Although it has been shown that the influence of the pressure drag increases when the density of the particles is similar to the density of the carrier phase [5], it decreases for low Reynolds numbers [50]. The present study is based on relatively low Reynolds numbers, and ultimately, the main objective of this paper is to shed light on the intermittency of sediment transport during the first stages of entrainment.

The presented approach is similar to cases of inertial particle transport in low Reynolds number flows [22], and two-way coupling simulations of sediment particles in turbulent flows [45]. The carrier phase equations are solved using a DNS approach developed by [43], whereas the dispersed phase equations are computed by coupling the DNS code to the open source, DEM-based LIGGGTHS package (see Appendix 1), which efficiently handles particle collisions and the computation of the forces in 4.

2.3 Computational setup

Our simulations are carried out in a rectangular flat-bed channel. The dimensions of the channel in the streamwise, spanwise, and vertical directions (x, y, z cartesian coordinates) are respectively $[x_L \times y_L \times z_L] = 0.12 \times 0.06 \times 0.04$ m. The boundary conditions consist of a no-slip rigid wall at the bottom, a zero-stress rigid lid at the top (i.e. free surface condition), and periodicity in the streamwise and spanwise directions. Spatial discretization in the x and y-directions is performed using a pseudospectral approach and derivatives in the z-direction are calculated via second order finite differencing. A computational grid of $128 \times 256 \times 128$ nodes is distributed uniformly in the x and y-directions and algebraically stretched in the z-direction. The size of the domain for the simulations presented in this investigation are based on the work of [45], who employed a computational domain of these dimensions to successfully study the mechanisms of bedload transport in similar conditions, with larger transport rates.

Time integration is performed using a third-order Runge-Kutta scheme for both the flow and dispersed phase equations (for details on the numerical methods and validation studies the reader is referred to the work of [43]. An additional validation of the coupling of the flow and particles solvers is shown in Appendix 2). The time step used for the flow, in Eq. 2, is equal to $\Delta t = 7.28 \times 10^{-4}$ s. The particle trajectories, on the other hand, are integrated using a time step of $\Delta t_p = 5.0 \times 10^{-7}$ s, owing to the requirement of resolving collision processes between particles. Thus for each time step of the flow solver, there are $\Delta t/\Delta t_p$ = 1456 time steps taken to integrate the equations of particle motion while assuming a frozen flow field. The total of simulation in all cases is roughly 120 s. The external pressure gradient added to 2 (f_i) is dynamically adjusted in order to obtain a desired bulk velocity which remains constant. As initial conditions, a fully developed unladen flow is used to initialize the flow field, into which the particles are inserted along the bottom wall with zero velocity.

To account for the effects of wall roughness, we insert "inactive" hemispherical particles at the wall, in a close-packed grid pattern. These particles remain stationary, do not couple onto the surrounding flow, but experience collisions with the "active" particles whose trajectories are being integrated in time according to 4, in order to generate roughness on the surface. This method of approximating wall roughness using inactive particles is similar to that of [52]. The radius of the inactive particles is set to $r^+_{inactive} = 3.44$, which is smaller than the viscous sublayer of wall-bounded turbulent flow where $r^+_{inactive} = (d/2)u^*/\nu$. In total we use 48, 510 spherical active particles and 4, 851 hemispherical inactive particles in all simulations. The setup of the computational domain, including the dimensions of the channel and details on the particles used in the simulations, is shown in Fig. 1.

Numerical simulations of the particle dynamics in this investigation are characterized by the Shields parameter θ, defined as follows,

$$\theta = \frac{\tau_0}{(\rho_s - \rho_f)gd} \tag{6}$$

where $\tau_0 = \rho_f u^{*2}$ is the averaged bed shear stress, and the other magnitudes have been defined previously. The critical magnitude of the Shields parameter, which is generally employed to establish the criterion for initiation of motion, is a function of the particle Reynolds number Re^*_p as shown in Fig. 2, and denoted as Shields' curve [51]. The magnitude of the drag force, on the other hand, is characterized by the particle Stokes number

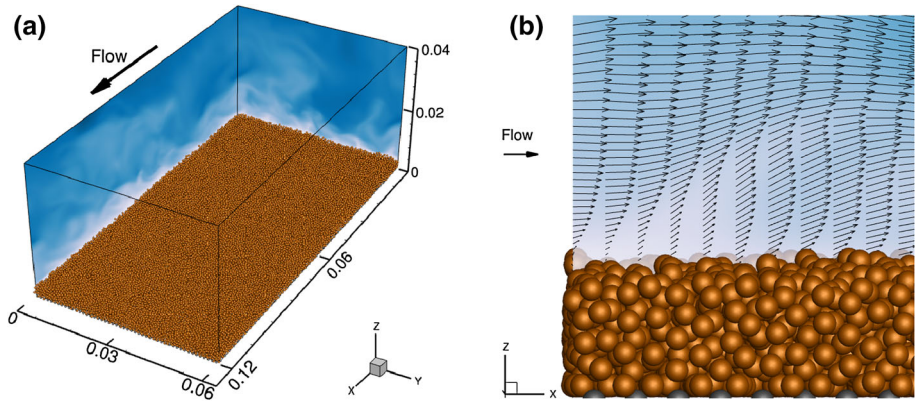

Fig. 1 (Color online) Snapshots of the flow and particles in the computational domain. **a** The complete computational domain corresponds to a rectangular channel with sediment particles initially at the *bottom* (the dimensions are shown in meters); and **b** Lateral view of a zoomed region near the *bottom* of the channel with instantaneous velocity profiles in a *vertical plane*. The bed is formed by a layer of many particles, with a thickness of approximately ~ 5 to 6 *d*. Active particles are *colored* in *brown*, and halves of inactive particles in *gray* are shown at the very *bottom*. *Blue/white contours* indicate streamwise velocity magnitude

St_k, which is defined as the ratio of the particle response time and the characteristic time scale of the flow as follows,

$$St_k = \frac{\rho_s d^2 U}{18 \rho_f \nu z_L} \tag{7}$$

where U and z_L are the bulk velocities of the flow and the water depth, respectively.

Since we are ultimately interested in the intermittency of sediment transport near the threshold of particle motion, six different cases are simulated, which span a range of the Shields parameter θ near the critical value, while maintaining a roughly constant particle Reynolds number Re_p^* and Stokes number St_k. Additionally, two extra cases are included far from the critical value of the Shields parameter. They are only used as extreme cases with continuous transport, focusing our study on the first six. All cases are shown by the red dots in Fig. 2. Parameters including the bulk flow Reynolds number ($Re = Uz_L/\nu$), collision properties (e.g., restitution coefficient, elasticity parameters, etc.), and Froude number ($Fr = U/\sqrt{gz_L}$) are held constant for all the simulations. The coefficient of restitution, Poisson's ratio, coefficient of friction and Young's modulus used in the simulations are characteristics for sand [32, 45]. The general parameters for all simulations are shown in Table 1, while conditions specific to each case are presented in Table 2.

Finally for measuring the sediment flux, which is a primary quantity of interest, a control plane is defined at the center of the channel whose normal vector is aligned with the streamwise direction. We then count the number of grains that cross the control plane during a given flow time step Δt. We do this for all time steps in the simulation, constructing the series of sediment transport as a function of time. In certain cases some particles cross the plane and rebound back upstream. In these cases we eliminate them by filtering the series, and eliminating negative fluxes across the plane. From the series we then compute the cumulative series of sediment flux $S(t)$, which provides the total number of particles that have crossed the control plane from the beginning of the simulation until

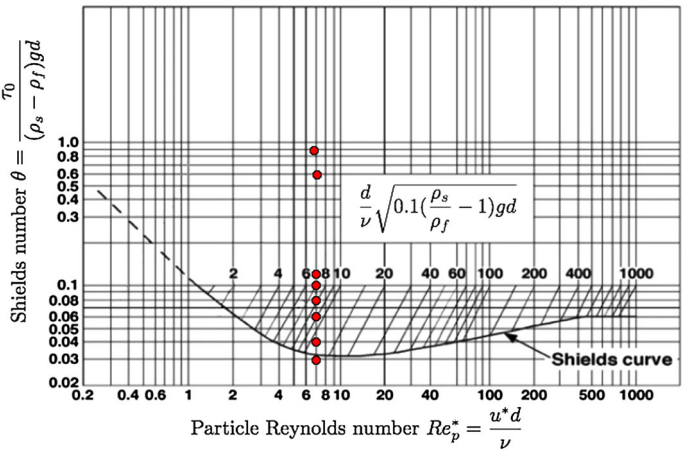

Fig. 2 (Color online) Shields diagram (after [51], modified from [18]) with the simulated cases in *red points*. These go from very near the threshold conditions of entrainment, defined by the *solid black Shields' curve*, to conditions where the sediment transport is strongly favored. The simulations for $\theta = 0.84$ and $\theta = 0.59$ (case 0-A and 0-B in Table 2) are extreme cases, used only as examples of a limiting case

Table 1 Constant flow conditions and particle properties for all the simulations

Parameter	Symbol	Value
Reynolds number	Re	3632
Froude number	Fr	0.15
Stokes number	St_k	$\sim$0.08 to 0.11 m/s
Bulk velocity	U	0.091 m/s
Friction velocity	u^*	$\sim$ 0.0081 to 0.0089 m/s
Fluid density	ρ_f	1000 kg/s
Kinematic viscosity	ν	1.003×10^{-6} m^2/s
Particle diameter	d	0.8 mm
Coefficient of restitution	e	0.01
Poisson's ratio	ϑ	0.45
Young's modulus	Y	2.5×10^7Pa
Coefficient of friction	μ_f	0.6

time t. This series $S(t)$ will play a central role in the analysis performed in the following section.

3 Results

In this section we analyze the results of the simulations by comparing the statistics of sediment dynamics for the parameter space defined in Subsect. 2.3. We calculate the histograms of particle velocities in three dimensions to investigate the characteristics of sediment motion near the critical Shields parameter. From the bed activity, defined as the

Table 2 Simulated cases

	Case 0-A	Case 0-B	Case 1	Case 2	Case 3	Case 4	Case 5	Case 6
Re_p^*	6.47	7.09	6.88	6.97	7.00	6.88	7.03	6.95
θ	0.84	0.59	0.12	0.10	0.08	0.06	0.04	0.03
ρ_s (kg/m^3)	1010	1017	1080	1096	1121	1161	1241	1347

We modify the density of the particles for each case in order to change the Shields parameter

number of active particles participating on bedload transport at any given instant in time, we identify a transition to a regime where there are always particles in motion, as the Shields number of the simulation increases. The particle trajectories are also used to obtain statistics of jump lengths in the streamwise direction, in terms of the Shields number. Finally, we analyze the intermittency of the cumulative bedload flux by characterizing the time series through the multifractal spectrum of sediment transport, which reveals the scaling of transport events for different Shields numbers.

3.1 Particle velocity distributions

We compute the probability density functions (pdfs) of particle velocities in each of the three spatial dimensions, i.e., longitudinal, spanwise and wall-normal, which are shown in Figs. 3, 4 and 5 respectively. The pdfs are constructed using the histograms of instantaneous particle velocities of all active particles based on all time steps over a given simulation.

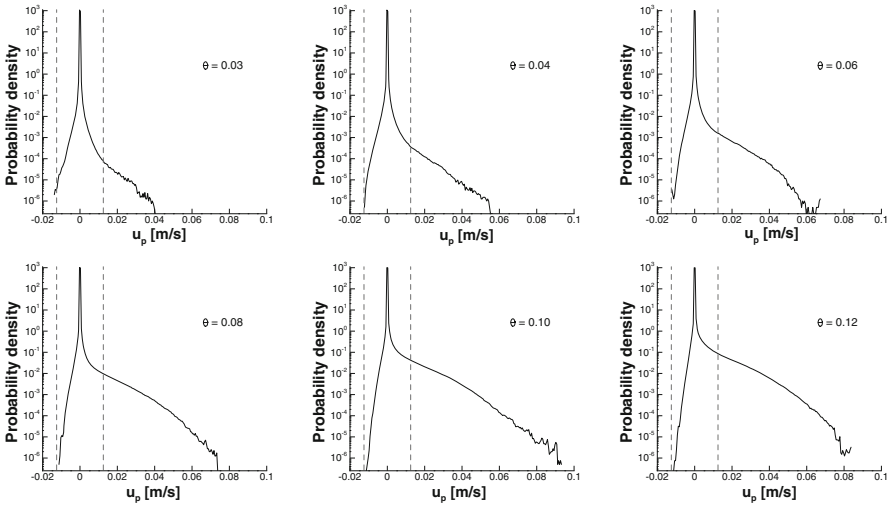

Fig. 3 Probability density functions of streamwise particle velocity for the Shields parameters of cases 1–6. The central region marked with *dashed vertical lines* corresponds to positive and negative values of the critical velocity v_{cr}, which is used to delineate particles considered in motion, which lie outside this region. The positive velocities show an exponential-like distribution after the cutoff, where a linear trend is visible in the semi-log scale

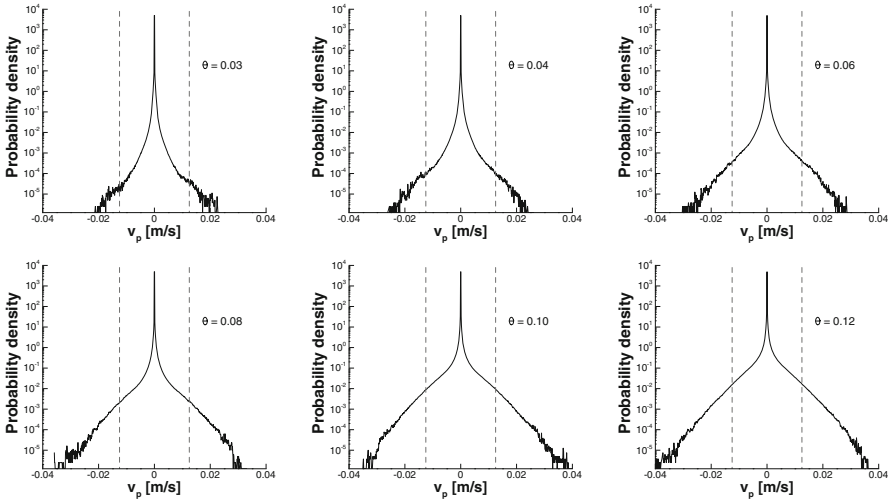

Fig. 4 Probability density functions of spanwise particle velocity for the Shields parameters of cases 1–6. The negative and positive tails are again exponential-like after the cutoff v_{cr} and are symmetric with respect to zero

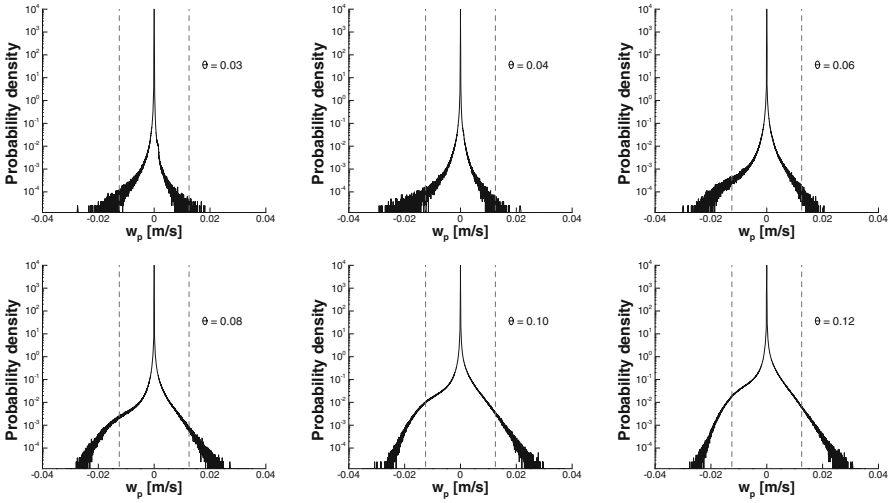

Fig. 5 Probability density functions of vertical particle velocity for the Shields parameters of cases 1–6. Negative and positive sides show contrasting behavior, revealing the dominance of different physical mechanisms in each region (gravity and drag force, respectively). Curves become *straight lines* in the semi-log scale as the Shields number increases, exposing a transition to an exponential-like distribution. This occurs faster for the *positive* velocities than for the *negative* ones

In Figs. 3, 4 and 5 we have marked a central section with dashed vertical lines, which is defined by the magnitude of a critical velocity $v_{cr} \approx 0.0125$ m/s. This critical velocity is set to delineate particles that we deem to be in active motion, compared for example with particles that could be simply rocking back and forth, or vibrating but not actively moving in the streamwise direction [34]. Such motions can occur when the local shear stresses that

come from the fluid are strong enough to move particles somewhat, but not sufficiently large to displace them downstream. While the choice of this value might be considered arbitrary, we selected its specific magnitude based on the experimental study of Roseberry et al. [44]. They experimentally investigated the bedload transport of coarse sand particles in a channel recording high-speed videos of grains in motion. This high-speed imaging was captured from a top view of the channel, with a spatial resolution of 1 pixel $\approx$ 0.05 mm and a time discretization of 250 frames per second. According to their set-up, they could not distinguish between two consecutive frames at velocities less than those permitted by the resolution of the images and its acquisition rate, i.e. $v_{cr} = 0.05$ mm/(1/250fps) = 0.0125 m/s. Under these assumptions, we are considering as modes of motion displacements by saltation, rolling, sliding, and in general, movements with a velocity greater than v_{cr}.

Figure 3 displays the pdfs for particle velocities in the streamwise direction for cases 1–6. In each figure, for all velocities greater than the critical velocity ($u_p > v_{cr}$), there appears to be an exponential-like tail in the distribution (straight line on a semi-log plot), which is in good agreement with findings from other studies [see 26, 44]. The size of this tail becomes stronger as the Shields parameter increases, in line with the idea that with increasing Shields number more particles become increasingly more mobile. The distribution in all cases is strongly skewed with a preferential motion in the direction of flow as one would expect. Note that with our choice of v_{cr} no particles appear to actively move in the backwards direction. The magnitude of the region between $\pm v_{cr}$ is dictated by the number of particles which remain at rest.

In the case of the spanwise particle velocity shown in Fig. 4, the particle velocity pdfs are completely symmetric, as one would expect since there is no preferential flow bias in this direction. Again, for $|v_p| > |v_{cr}|$ the probability densities display an almost exponential-like decay, while they are sharply peaked around 0. As the Shields number increases the exponential tails become stronger, as a greater fraction of the particles are mobilized. Indeed for the smallest Shields number, velocities greater than the critical velocity are within the noise of the distribution and practically speaking, the vast majority of particles are immobile. For $\theta = 0.03$, around 99.99 % of particles lie inside this region during the entire simulated period.

In Fig. 5 we report the pdfs for the vertical particle velocities, which also display many of the aforementioned features of the streamwise and spanwise velocities. One feature that is noteworthy is that the distributions are not symmetric as the mechanisms that induce upward and downward motions are not the same (drag and submerged gravity). In this sense we can compute the probability of having a positive or negative value of w_p depending on the Shields number, and we observe that those probabilities become more similar as the Shields number is increased, as shown in Table 3. These results suggest that at high Shields numbers, the motion in both vertical directions is dominated by the same physical mechanisms, contrary to the cases with low Shields numbers.

Finally for each of the particle velocity pdfs, we compute the skewness and plot it as a function of θ in Fig. 6. For the simulated cases, the values of the skewness of u_p are always positive, with a maximum value located at $\theta \approx 0.10$. The skewness approaches zero at high and low Shields parameter values, respectively, as a result of: (i) streamwise particle velocities gradually deviating from the mean in a symmetric way at high Shields parameters and (ii) a reduction in the number of particles participating in transport at low values. The skewness of v_p does not vary with the Shields parameter, owing to the statistical invariance with streamwise direction. The magnitude of the skewness of w_p decreases as

Table 3 Ratio between the probability of having $w_p \geq 0$ and $w_p < 0$

θ	$P(w_p \geq 0)/P(w_p < 0)$
0.03	1.227
0.04	1.220
0.06	1.160
0.08	1.136
0.10	1.104
0.12	1.077
0.59	1.062
0.84	1.084

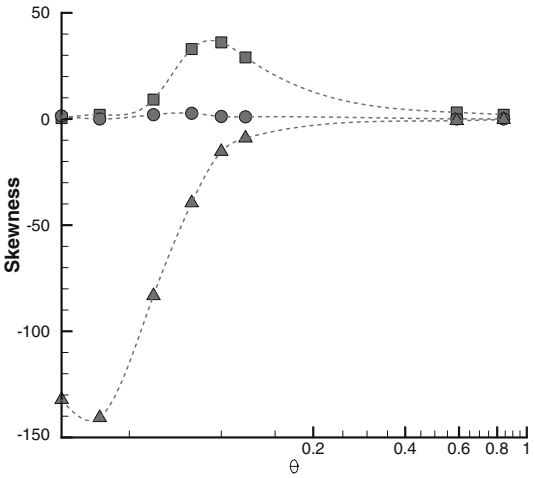

Fig. 6 Skewness of the particle velocity components as function of the Shields parameter. The *symbols black square*, *circle* and *black triangle* represent u_p, v_p and w_p, respectively. *Dashed lines* are spline fits over $log_{10}\theta$, to show the tendencies of the skewness

the Shields parameter increases, in accordance with the ratios of probabilities for positive and negative w_p discussed above regarding Table 3.

3.2 Activity

While knowing the detailed velocity distributions is useful, we also consider another more revealing metric that is commonly employed in sediment transport formulas: At any given time, how many particles are participating in transport in our system? This is quantified by the activity, defined as the number of particles in motion at a given instant in time. A similar definition for the activity has been given by Roseberry et al. [44], with the only difference that they considered the number of particles in motion per unit of bed area. Similar to the previous analysis of pdfs of particle velocity, the criterion for being in motion is that the velocity magnitude of a particle is greater than the aforementioned critical velocity ($\sqrt{u_p^2 + v_p^2 + w_p^2} \geq v_{cr}$). In this way, a particle moving in any direction (i.e., not just the streamwise direction) is counted as moving.

Thus each time step represents an instantaneous sample, and from the full time series a probability density function can be constructed for activity at each value of Shields

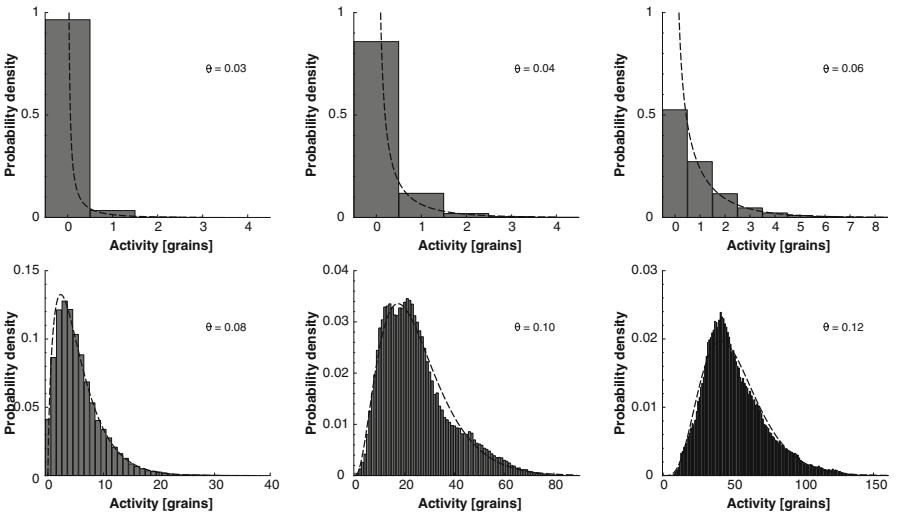

Fig. 7 PDFS of the activity, which is the total number of particles in motion at a given time inside the domain. The pdfs represent the probability of finding a determined number of particles in motion in a given time. *Dashed lines* are best fits to these using a gamma distribution

parameter. The pdfs for activity for cases 1–6 are shown in Fig. 7. In addition to the discrete probability density portrayed in this figure, we overlay the statistics of the numerical simulation with the best-fit of a Gamma distribution function:

$$f(\mathcal{X}|k,\beta) = \frac{1}{\beta^k \Gamma(k)} \mathcal{X}^{k-1} e^{\frac{-\mathcal{X}}{\beta}}. \tag{8}$$

The Gamma distribution is controlled by two parameters, k and β. Note that this is a continuous, rather than discrete distribution; previous studies have observed a negative binomial distribution fit to their data for activity [4], which is the discrete counterpart to the Gamma distribution. We also obtain excellent fits with the negative binomial, but choose to display the continuous Gamma for a specific reason explained below.

Qualitatively, the distributions in Fig. 7 can be broken into two subclasses. In the top row, corresponding to the smaller Shields parameter values, the best fit Gamma distribution falls into its exponential behavior regime, meaning that the largest probability is always associated with an activity of zero—i.e., that there is a strong probability that zero particles are moving during the entire period of simulation. This probability is greatest for the smallest Shields parameter, as depicted in the first plot of Fig. 7, which is in line with our intuition that smaller Shields parameters reflect less motion and more stationary particles. However in the bottom row, for larger values of the Shields parameter, the best fit Gamma distribution has transitioned to its other typical behavior, which is qualitatively more like a log-normal distribution. For this case there is zero probability that at any given time no particles are in motion—i.e., at least some particles are always in a state of motion.

Quantitatively this transition can be understood by exploring how the parameters of the Gamma distribution, k and β, evolve with the Shields parameter. For cases 1–6 these relationships are shown in Fig. 8. As noted qualitatively above, when $k<1$ the Gamma distribution looks like an exponential distribution, while for $k > 1$ it falls into its other, more log-normal behavior regime. Thus the value $k = 1$ sets a transition in behavior when

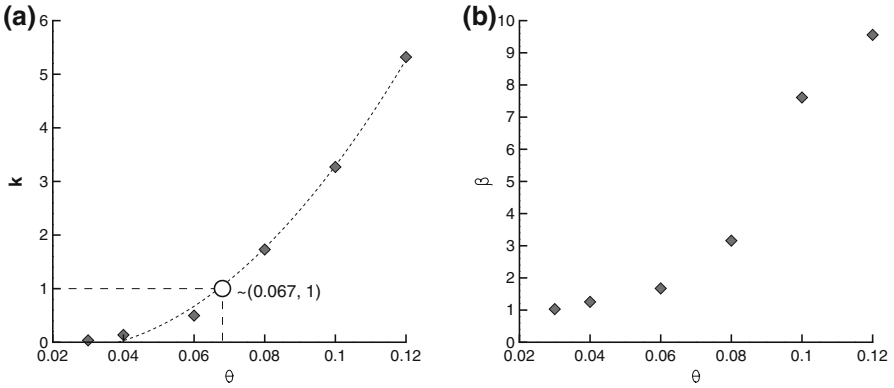

Fig. 8 Parameters k and β of the gamma distribution, used to fit the activity pdfs in Fig. 7, vs the Shields parameter. When $k \geq 1$ the Gamma distribution suggests that there are never times when all particles are in a state of rest and at least some are in motion. This occurs for Shields numbers $\theta \geq 0.067$

one might expect there to be times when there are no particles actively moving, versus a regime where there will always be at least some particles moving. An interpolation of the k parameter with these results suggests that the transition occurs at around $\theta = 0.067$, as shown in Fig. 8(a). Thus, while the critical Shields number for motion is around $\theta \approx 0.033$ (see the critical Shields parameter in the diagram shown in Fig. 2), our simulations show that a value roughly twice as large is needed to ensure that some sediment particles are always in motion. Continuously increasing k with Shields number, increases the skewness of the distribution and places a heavier weight on the power-law tail associated with larger activities. Likewise the monotonic relationship between β and Shields parameter in Fig. 8(b) implies that the mean of the distribution increases and that the exponential tempering happens at a larger value of activity. This is again in line with physical reasoning that a greater Shields parameter means more particles in motion and thus greater activities.

3.3 Travel distance statistics

When developing a Lagrangian picture of how sediment particles move, so as to ultimately build an upscaled/effective model for transport, it is important to have an understanding of the particle travel (or jump) statistics in addition to mere particle activity; that is, what is the statistical distribution of travel distance when particles become dislodged from the bed? Such information, combined with generalized central limit theorems under certain simplifying assumptions, can yield macroscopic equations for transport, as stated in the original work of Einstein [21]. While the specific focus of this paper is not yet at this model development stage, we present these statistics here so that they might be used for this end goal in the future. Additionally they provide useful information in addressing some of the questions we pose here relating to intermittency, as particle jump statistics and intermittency are often tightly linked [e.g., 19].

Considering sediment transport as a series of consecutive cycles of particle resting and motion, we gather statistics on the distance that the particles travel downstream during a given transport event; we denote these distances as λ. Since in this instance we are only concerned with streamwise particle movement, we limit our presentation to positive values

of λ; we consider a particle to be in a state of motion when its streamwise velocity surpasses the critical velocity ($u_p \geq v_{cr}$), and thus λ is computed as the difference between the final and initial x-position of the grains between two consecutive stop events.

Pdfs of λ across the range of considered Shields numbers in cases 1–6 are shown in Fig. 9. Consistent with the above discussions, higher Shields parameters result in a broader distribution of jump lengths. Starting at case 1, where $\theta = 0.03$, the largest jump length measured was only 3 particle diameters in length. As θ is increased, nonzero probabilities of travel distance as high as 50 particle diameters are found, illustrating that higher bed stresses result in both increased jump activity as well as flight distance. The shape of the travel distance pdfs shown in Fig. 9 remained generally constant, with the peak length always around a single diameter

3.4 Characterization of the intermittency in the bedload transport flux

At low Shields numbers, the complex interactions of the sediment particles with the turbulent boundary layer produce a highly intermittent bedload transport flux. We perform a statistical analysis of this intermittency using our measured cumulative bedload transport flux $S(t)$, which is calculated following Escauriaza and Sotiropoulos [23]. We define a cross section in the channel, and compute the time series of the number of sediment particles that cross this vertical plane at every instant in time. Figure 10a depicts the cumulative bedload transport $S(t)$, for four different Shields numbers, showing a highly irregular flux with multiple transport events of different magnitudes, and a seemingly random series of plateaus that correspond to time intervals with no particles crossing the control plane. As shown qualitatively in Fig. 10b, the cumulative bedload flux in these cases exhibits self-similarity, with a repeating structure of transport episodes and plateaus as we magnify the curve to observe the transport at smaller time scales. This intermittent and self-similar flux in time corresponds to the fractal curve known as the devil's staircase [see Refs. 22, 23, for details].

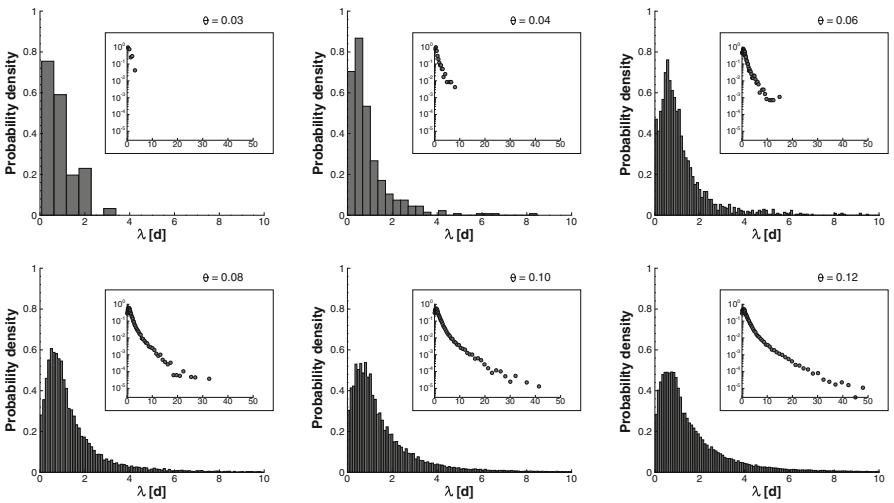

Fig. 9 PDFs of travel distance of the particles in diameter units. *Subplots* show the same pdfs in semi-log *scales* and for a longer interval of λ

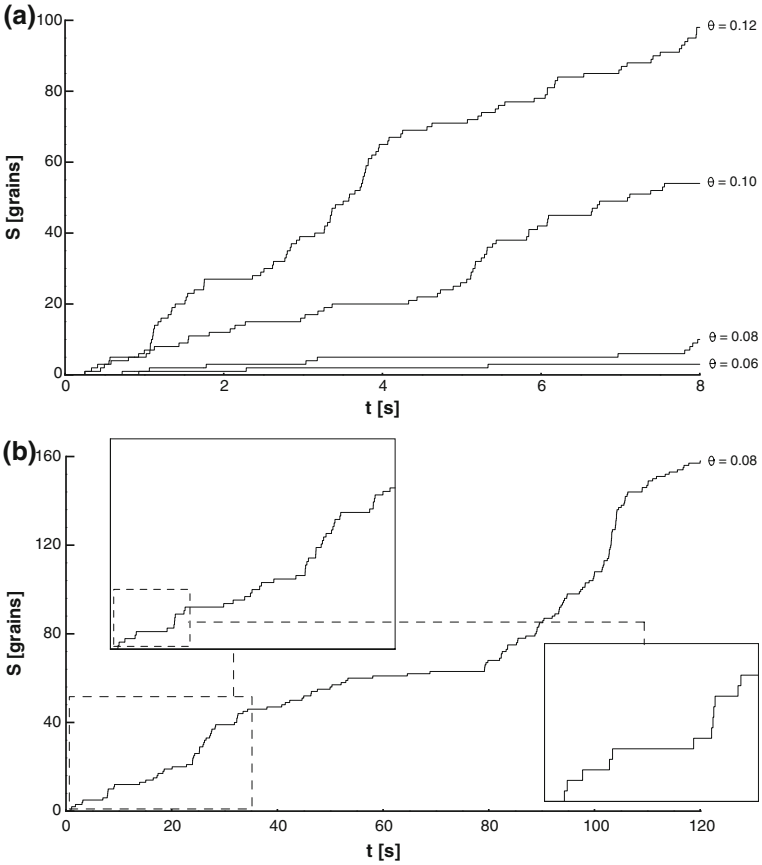

Fig. 10 **a** Cumulative sediment transport for several Shields parameters (not all cases are shown). **b** Cumulative sediment transport at different *scales* qualitatively showing self-similarity for $\theta = 0.08$

The occurrence of bedload transport events for low Shields is characterized by the fractal dimension of the devil's staircase, and the scaling of events of different magnitudes by the multifractal spectrum of the flux. In what follows we describe briefly the methodology to analyze the intermittency of bedload transport through the multifractal or singularity spectrum of $S(t)$, and study the evolution of these statistics as the Shields number increases.

3.4.1 Fractal dimension and multifractal spectrum of the bedload flux

The distribution of all the transport events in time, seen at different time scales in a self-similar bedload flux, is characterized by the fractal dimension of the curves shown in Fig. 10. Here we follow the classical methodology employed by Bak [6] to compute the fractal, Hausdorff, or box-counting dimension of the devil's staircase [see also 23]. If we define the time scale as the product of an integer r and the time-step of the simulation Δt, we can calculate the total width of periods with no transport that are larger than $r\Delta t$, defined as $T(r\Delta t)$. Subsequently, we compute the episodes of transport as the spaces between the plateaus that can be identified at that time scale during the total time of

computation T_{max}. We then measure this quantity to obtain the total number of time windows $N(r\Delta t)$ with magnitude $r\Delta t$, required to contain all the segments previously calculated, as follows,

$$N(r\Delta t) = \frac{T_{max} - T(r\Delta t)}{r\Delta t}. \tag{9}$$

Therefore, the fractal dimension of the bedload transport events, D_0, corresponds to the exponent of the power-law distribution that characterizes the scale-invariance of the flux, such that,

$$N(r\Delta t) \sim \left(\frac{1}{r\Delta t}\right)^{D_0}. \tag{10}$$

If we now calculate the scaling regime of the occurrence of events of different magnitudes, seen at the time scales given by $r\Delta t$, we will find a range of exponents represented by the singularity or multifractal spectrum of bedload transport. We first compute the number of grains that cross the reference plane between two consecutive plateaus of the devil's staircase, denoted as i and $i-1$. This value corresponds to the transport event magnitude, which we divide by the total number of particles that have crossed the plane by the end of the simulation, $S(T_{max})$, as follows,

$$\mu_i(r\Delta t) = \frac{S_i(r\Delta t) - S_{i-1}(r\Delta t)}{S(T_{max})}, \tag{11}$$

where $\mu_i(r\Delta t)$ is thus a measure of the normalized strength of the transport event occurring between two inactive periods. As explained by Harte [28], the q-th order statistical moment of $\mu_i(r\Delta t)$, denoted as $M(q, r\Delta t)$, can also be represented by a power-law relationship if the moment distributions are self-similar, such that the following expression is valid for each value of q,

$$M(q, r\Delta t) \sim (r\Delta t)^{\zeta(q)}, \tag{12}$$

where $\zeta(q)$ is called the scaling exponent function. If $\zeta(q)$ has a linear dependence on q, the series is monofractal only characterized by the exponent D_0. On the other hand if $\zeta(q)$ has a non-linear dependence on q, the series is defined as multifractal. In the latter case, the measure $\mu_i(r\Delta t)$ locally scales with $r\Delta t$, through the so-called Hölder exponent α, which is also called the singularity strength at scale $r\Delta t$,

$$\mu_i(r\Delta t) \sim (r\Delta t)^{\alpha}. \tag{13}$$

This exponent characterizes the local differentiability of the measure, since values of $\alpha < 1$ imply that the series is not differentiable at that point. If α tends to one, on the other hand, the series is "smoother", and can be differentiable when it reaches a value equal to 1. The exponent $f(\alpha)$ is therefore defined as the fractal dimension of the set of singularities with scaling index α, which yields the multifractal or singularity spectrum $f(\alpha)$ vs α. The exponents $f(\alpha)$, α, $\zeta(q)$, and the moment order q, are related through the Legendre transform, which is used to calculate the multifractal spectrum [25],

$$\begin{aligned} \alpha &= \frac{d\zeta(q)}{dq} \\ f(\alpha) &= q\alpha - \zeta(q), \end{aligned} \tag{14}$$

The maximum value of the multifractal spectrum $f(\alpha)$ is equal to the fractal or box-counting dimension of the bedload flux, D_0, and it can be used to quantify the intermittency of the bedload flux in time. When more particles are continuously crossing the control plane, with events that are observed at finer time-scales, the fractal dimension of the time series approaches 1, $D_0 \rightarrow 1$. Conversely, as the duration of the plateaus increases, D_0 tends to zero due to the more intermittent sediment transport events. For more details on the basic aspects of the multifractal theory, the reader is referred to [23, 25, 28, 46].

3.4.2 Evolution of intermittency for increasing Shields numbers

As previously discussed, Fig. 10a displays the cumulative bedload transport flux $S(t)$ for four values of the Shields parameter, showing also the self-similar structure of these curves. Fig. 10b presents $S(t)$ for a single case, but covering the entire time duration of the simulation. All cases in the range $\theta = 0.06-0.12$ display intermittency, and follow a characteristic devil's staircase structure. However, the degree of intermittency appears to differ considerably, as the duration of the plateaus shortens with an increasing Shields number. For the case with the maximum Shields number simulated, $\theta = 0.84$, the bedload flux becomes a continuous function of time, and $S(t)$ increases continuously with no plateaus and $D_0 = 1$ (not shown here). This result indicates that for large values of θ there are always sediment particles crossing the vertical plane, which can be measured for all the range of time scales analyzed. For the smallest Shields numbers ($\theta = 0.03$ and 0.04) very few particles are mobile, while in the range of $\theta = 0.06-0.12$, the intermittent-like behavior is clearly observed.

Figure 11 shows the singularity spectra for the four values of θ near the threshold of motion (cases 1–4), which are calculated using the statistical moments of transport events and the Legendre transform, Eq. (14). The spectra follow a non-monotonic single peaked pattern, similar to that observed in the work of Escauriaza and Sotiropoulos [23]. The corresponding fractal dimensions (peaks of the spectra) are shown in the adjacent plot with a clear monotonic increasing trend, in which the values of D_0 increase with the Shields number. For the extreme case of $\theta = 0.84$, the fractal dimension has actually saturated, yielding a continuous flux with $D_0 = 1$. Based on this data alone, we can anticipate that the fractal dimension will saturate at a value of around $\theta = 0.59$, above which no intermittency

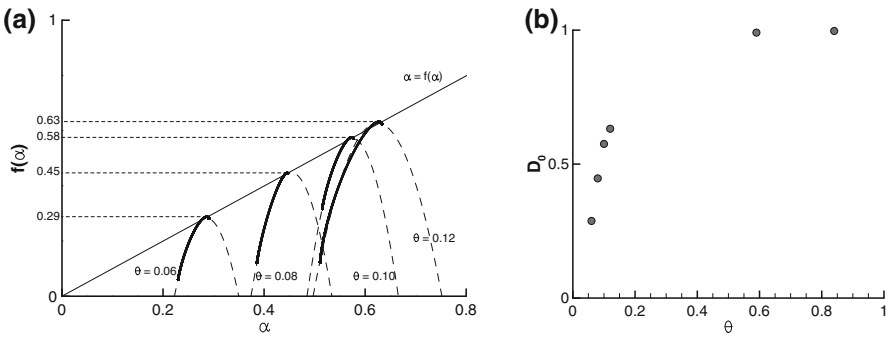

Fig. 11 **a** Singularity spectra $f(\alpha)$ for $\theta = 0.06-0.12$ showing the multifractal nature of the sediment transport near the threshold of motion. The *bold curves* are the computed region of the spectra, which are filled with symmetrical quadratic fits (*dashed curves*). The spectra are tangent to the line $f(\alpha) = \alpha$. **b** Fractal dimensions of the sediment transport as a function of the Shields parameter

will occur. Finally, it is also important to point out that as the Shields number increases the spectra move toward larger values of α, becoming more continuous. They also encompass a wider range of α, which means that in these cases there is a wider range of transport event magnitudes.

4 Conclusions

In this investigation we performed simulations of sediment transport in a flat-bed channel using a Lagrangian particle model based on the DEM approach, coupled with direct numerical simulations for the fluid flow. By fixing a constant particle Reynolds number Re_p^*, and varying the Shields parameter θ, we studied eight cases encompassing a range from almost no sediment motion to continuous entrainment. This research is mainly focused on the dynamics of the cases that are near the threshold of motion to study the statistical characteristics of particle velocities, bed activity, and jump length size of the particles. For the lower Shields numbers, we find that the bedload transport flux is highly intermittent and that it can be characterized by the multifractal spectrum of transport events. The intermittency and fractal properties are lost as the Shields parameter increases, producing series of continuous particle transport in time.

For larger magnitudes of the Shields parameter, particles become easier to dislodge by the turbulent coherent structures of the boundary layer flow, exposing the particles to higher stresses and mobilizing a larger portion of the bed. This favors the emergence of a continuous bedload transport flux, which is quantified by observing that the multifractal behavior breaks down at some point in the interval $\theta \approx 0.12-0.59$ of the Shields parameter, when $Re_p^* \approx 7.0$. An additional transition of the intermittent dynamics is also observed for the range of times scales analyzed in our research (from the time step of the calculation to the total time simulated). At a value of the Shields parameter $\theta \approx 0.067$, we observed on the pdfs of particle activity that the probability of finding zero moving particles abruptly transitions to zero for the total time period that was simulated. However, at these stages the existence of plateaus in the sediment transport flux persists over this critical value of θ, i.e. jumps are short and they not necessarily reach the control plane for particles actively participating in transport.

A principal finding of this research is that a Lagrangian model coupled with DNS can capture the intermittent nature of the sediment transport presented during the first stages of the entrainment. Taking into account the restriction on motion that particles impose on each other, the model must include the computation of collisions between grains. A two-way coupling approach should be chosen if the studied bed is composed of many layers of particles.

The devil's staircase distributions correspond to an aggregated manner of conceiving the individual trajectories of the particles with a given distribution of resting times. For example, if greater resting times are likely, this fact will be indirectly expressed by longer plateaus in the associated devil's staircase. A suitable conceptual model for understanding the behavior of these trajectories has been proposed by Nikora et al. [41] and experimentally studied by Campagnol et al. [11]. They divided the time scales of the trajectories into three categories: a local range for the smallest time scales, an intermediate range, and a global range. At the same time, the local range can be split into two subdivisions: a local-near field range and a local-ballistic range [8, 10, 11]; whereas a transition regime can be identified between the intermediate and global ranges [10]. Each of these categories is

characterized by a different diffusion regime, i.e., a normal or anomalous regime in the Fickian sense. Given that the fractal dimension contains information for all the scales, it could be potentially used for deriving the different diffusion regimes in time (or vice versa). This approach is proposed for future research. Additionally, it is important to note that in the model of Nikora et al. [41], the variance of the particle displacements increases with time at a different rate depending on the diffusion regime. In this sense, throughout our simulations we have observed transitions among these regimes, where the variances increase homogeneously in time as the Shields number is also increased. These phenomena could be directly related to changes in the distributions of the particles resting times and travel distances, which are the variables highlighted by Bialik et al. [10]. Nonetheless, these are preliminary results (not included in this article), which need a deeper study to be confirmed.

Finally, let us note that the Shields curve is roughly independent of Re_p^* in the range $Re_p^* \approx 6-20$, i.e. here the initiation of motion only depends on θ as the flow becomes fully rough (c.f. Fig. 2). Under this premise, one could speculate that the results presented through this investigation are valid for the entire mentioned range. However, additional research must be conducted to validate this point. In future investigations we will address important issues to characterize bedload transport, exploring the phase-space of parameters to understand the specific influence of the time scales of the turbulent flow on particle motion, and incorporate different particle sizes in the simulations to study the effects of grain size distributions on the flow and on particle interactions.

Acknowledgments This work has been supported by Fondecyt Project 1130940, ONR-G NICOP N622909-11-1-7041, and Conicyt/Fondap Grant 15110017. C. González acknowledges the funding from the Ph.D. National Grant Conicyt-21120939. S. Bateman and J. Calantoni were supported under base funding to the Naval Research Laboratory from the Office of Naval Research.

Appendix 1

The discrete element method (DEM) used for the computation of the particles dynamics is the open source LIGGGHTS, available on http://www.liggghts.com. The equations solved by this algorithm have been previously explained by Chand et al. [16] and Schmeeckle [45], but following their work and for the clarity of the reader, we repeat them here.

For each particle, collisions with other grains are computed when the distance between their center is less or equal than the sum of their radii, i.e. they overlap, or at least, they are in contact. For two particles, the force product of their collision is divided into a normal force (F_n) and a tangencial force (F_t):

$$F^{col} = F_n + F_t \tag{15}$$

The normal force along the line of center between two colliding particles is computed as:

$$F_n = K_n \delta_n - \gamma_n v_n \tag{16}$$

whereas the tangencial force is calculated as follows:

$$F_t = K_t \delta_t - \gamma_t v_t \tag{17}$$

where K_n and K_t are the stiffness coefficients, δ_n and δ_t are the overlap distance between

two grains, γ_n and γ_t are the viscoelastic damping constants, v_n and v_t the relative velocity and the subscripts n and t correspond to the normal and tangencial components. If necessary, the tangential overlap is truncated in order to satisfy the condition $F_t \leq \mu_f F_n$, where μ_f is the coefficient of friction. In turn, the previous variables are computed as follows:

$$K_n = \frac{4}{3} Y^* \sqrt{R^* \delta_n} \tag{18}$$

$$\gamma_n = -2\sqrt{\frac{5}{6}} B \sqrt{S_n m*} \geq 0 \tag{19}$$

$$K_t = 8G^* \sqrt{R^* \delta_n} \tag{20}$$

$$\gamma_t = -2\sqrt{\frac{5}{6}} B \sqrt{S_t m^*} \geq 0 \tag{21}$$

The parameters in Eqs, 18–21 are defined as follows:

$$S_n = 2Y^* \sqrt{R^* \delta_n} \tag{22}$$

$$S_t = 8G^* \sqrt{R^* \delta_n} \tag{23}$$

$$B = \frac{\ln(e)}{\sqrt{\ln^2(e) + \pi^2}} \tag{24}$$

$$\frac{1}{Y^*} = \frac{1 - \vartheta_1^2}{Y_1} + \frac{1 - \vartheta_2^2}{Y_2} \tag{25}$$

$$\frac{1}{G^*} = \frac{2(2 + \vartheta_1)}{Y_1} + \frac{2(2 + \vartheta_2)}{Y_2} \tag{26}$$

$$\frac{1}{R^*} = \frac{1}{R_1} + \frac{1}{R_2} \tag{27}$$

$$\frac{1}{m^*} = \frac{1}{m_1} + \frac{1}{m_2} \tag{28}$$

where e is the coefficient of restitution, ϑ is the Poisson's ratio, Y the Young's modulus, R the radius of a particle, m the mass of a particle and the subscripts 1 and 2 are the identifiers for two particles in contact.

Appendix 2

In this appendix we present a validation of the coupling between the fluid and solid phases. The numerical method for the fluid solver has already been validated before [see for example 43]. Also, the dispersed phase solver has been broadly used and validated in several previous investigations [16, 26, 45].

In order to carry out the validation, we perform additional simulations of a flow over a flat bed channel, different than those presented in this article. The setup reproduces the

Table 4 Particles parameters of comparison cases

Parameter	Reference cases Schmeeckle [45]	Comparison cases
Diameter (mm)	0.5	0.5
Density (kg/m^3)	2650	2650
Coefficient of restitution	0.01	0.01
Poisson's ratio	0.45	0.45
Young's modulus (Pa)	0.5×10^6	0.5×10^6
Coefficient of friction	0.6	0.6

simulations carried out by Schmeeckle [45]. The configuration of the system is a rectangular channel of 0.12 m long, 0.06 m wide and 0.04 m deep. The mean velocities of the considered cases for comparisons are $U = 0.2$, 0.3, 0.4 and 0.5 m/s. Let us note that given these high velocities, here our algorithm works as a LES model with numerical dissipation instead of a DNS one (for this approach, see for example [33]). Following the reference case, our flow is driven by a pressure gradient, with periodic lateral boundary conditions, a free-slip rigid lid at the top, a solid wall at the bottom, and a two-way coupling approach.

Schmeeckle [45] used 115, 728 spherical particles with a diameter $d = 0.5$ mm, which corresponds to 7.57 cm^3 of solid material. We consider 28, 800 hemispherical particles stuck to the bed in order to have static particles at the bottom. In this way, we fulfill the condition used by [45] of particles with almost zero velocity at the bottom. Furthermore, we use 101, 328 spherical mobile particles. The diameter that we use is the same that the reference case. According to these conditions, the solid material of our simulations is 7.57 cm^3, coinciding with the value employed by [45]. More parameters of these simulations are shown in Table 4.

A comparison of the bulk velocity profiles of the flow in the downstream direction is shown in Fig. 12a. The concentration of particles in the vertical direction is also compared in Fig. 12b. These results show that our model captures the region of slower flow velocity in and near the sediment bed, the development of the logarithmic velocity profile, and the distribution of particles in the vertical direction, which is directly related to the fluid-particle interactions.

Additionally, we compare the velocity profile for a bulk velocity $U = 0.2$ m/s using a one-way and two-way coupling approach (shown in Fig. 13). For the one-way coupling case, the profile matches theoretical curves (see 29). From the perspective of the flow, this is similar to the boundary layer flow without sediments. Even though 29 can be used to calculate separately every region of a velocity profile without sediment particles [49, 54], the equation for the buffer layer can represent the whole inner layer accurately [48]. Here, the inner layer is composed by the viscous, buffer, and logarithmic layers. This equation is also known as the Spalding's law of the wall [54] and we use it for the range $0 \leq z^+ \leq 350$. We use the outer-layer equation from 29 outside this range [13].

$$\frac{U}{u^*} = \begin{cases} z^+ & \text{if } z^+ \leq 5 \quad \text{Viscoussublayer} \\ z^+ - e^{-\kappa B}\left[e^{\kappa u^+} - 1 - \kappa u^+ - \dfrac{(\kappa u^+)^2}{2} - \dfrac{(\kappa u^+)^3}{6}\right] & \text{if } 5z^+ \leq 30 \quad \text{Bufferlayer} \\ \dfrac{1}{\kappa}\ln z^+ + B & \text{if } 30 < z^+ \leq 350 \quad \text{Log.layer} \\ \dfrac{1}{\kappa}\ln z^+ + B + \dfrac{2\Pi}{\kappa}\sin^2\left(\dfrac{\pi}{2}\dfrac{z}{\delta}\right) & \text{if } 350 < z^+ \leq 1750 \quad \text{Outerlayer} \end{cases} \tag{29}$$

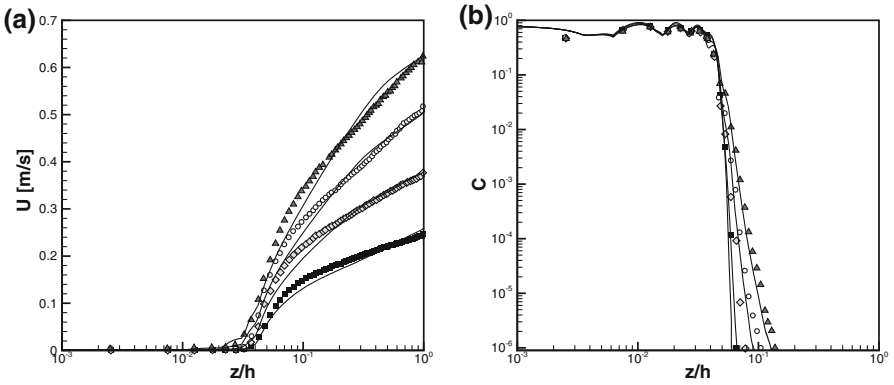

Fig. 12 Comparison of bulk velocity profiles of the flow (U) and volumetric concentration of particles (C). The *horizontal axis* corresponds to the non-dimensional *vertical* coordinate by the channel depth. Data extracted from [45] are plotted as *black square*, *soft gray diamond*, *white circle* and *gray triangle* and they represent U = 0.2, 0.3, 0.4 and 0.5 m/s respectively. *Continuous lines* are our simulated results. **a** In the original plot from [45], the bulk velocity was divided by the friction velocity. We extract it from the plot in order to directly compare the flow field. **b** Concentration is in volume of particles divided by volume of fluid

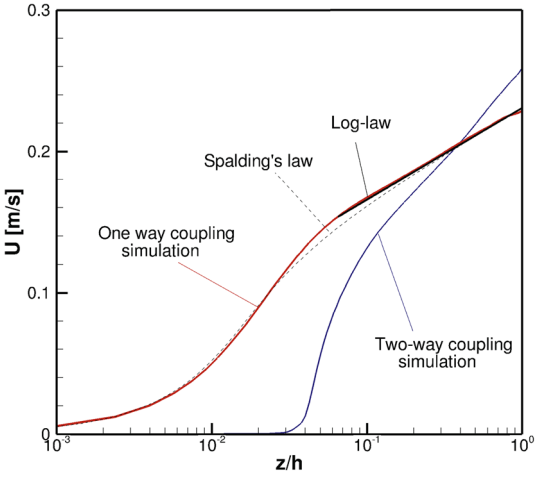

Fig. 13 (color online) Bulk velocity profile for U = 0.2 m/s. *Red line* corresponds to simulations with a one-way coupling approach, whereas the blue line corresponds to simulations with a two-way coupling approach. In *black line* the log-law is plotted and in *dashed line* the Spalding's law is plotted [48, 49, 54]. The consideration of the two-way coupling approach yields to a completely different development of the bulk velocity profile

In 29, u^* is the friction velocity, $z^+ = \frac{zu^*}{\nu}$, ν is the kinematic viscosity, $u^+ = \frac{U}{u^*}$, δ is the boundary layer thickness, $\kappa = 0.41$ is the von Kármán constant, $\Pi = \frac{\kappa A}{2}$ and A and B are experimental coefficients with $A = 2.5$ for flat plates and $B = 5.0$ [14]. In the outer-layer we use the approximation $\delta \approx 1750 \frac{\nu}{u^*}$ [54].

References

1. Adrian RJ (2007) Hairpin vortex organization in wall turbulence. Phys Fluids 19(4):041301
2. Allen JRL (1971) Bed forms due to mass transfer in turbulent flows: a kaleidoscope of phenomena. J Fluid Mech 49(1):49–63

3. Alletto M, Breuer M (2012) One-way, two-way and four-way coupled LES predictions of a particle-laden turbulent flow at high mass loading downstream of a confined bluff body. Int J Multiph Flow 45:70–90
4. Ancey C, Böhm T, Jodeau M, Frey P (2006) Statistical description of sediment transport experiments. Phys Rev E 74(1):011302
5. Armenio V, Fiorotto V (2001) The importance of the forces acting on particles in turbulent flows. Phys Fluids 13(8):2437–2440
6. Bak P (1986) The Devil's staircase. Phys Today 39:38–45
7. Balachandar S (2013) Particle-laden flows. In: Fernando HJS (ed) Handbook of environmental fluid dynamics, vol 1. CRC Press/Taylor & Francis Group, New York. LLC. ISBN: 978-1-4398-1669-1
8. Ballio F, Campagnol J, Nikora V, Radice A (2013) Diffusive properties of bed load moving sediments at short time scales. In: Proceedings of 2013 IAHR world congress, Chengdu, China (CD)
9. Bialik RJ (2013) Numerical study of near-bed turbulence structures influence on the initiation of saltating grains movement. J Hydrol Hydromech 61(3):202–207
10. Bialik RJ, Nikora V, Karpiński M, Rowiński P (2015) Diffusion of bedload particles in open-channel flows: distribution of travel times and second-order statistics of particle trajectories. Environ Fluid Mech 15(6):1281–1292
11. Campagnol J, Radice A, Ballio F, Nikora V (2015) Particle motion and diffusion at weak bed load: accounting for unsteadiness effects of entrainment and disentrainment. J Hydraul Res 53(5):633–648
12. Clift R, Grace J, Weber M (1978) Bubbles, drops, and particles. Academic Press, New York
13. Coles DE (1956) The law of the wake in the turbulent boundary layer. J Fluid Mech 1:191–226
14. Coles, DE, Hirst EA (1968) Computation of turbulent boundary layers. In: Proceedings AFOSR-IFP Stanford Conference, Stanford University, Stanford, California, vol 2
15. Crowe CT, Troutt TR, Chung JN (1996) Numerical models for two-phase turbulent flows. Annu Rev Fluid Mech 28(1):11–43
16. Chand R, Khaskheli MA, Qadir A, Ge B, Shi Q (2012) Discrete particle simulation of radial segregation in horizontally rotating drum: effects of drum-length and non-rotating end-plates. Phys A 391(20):4590–4596
17. Chang Y, Scotti A (2003) Entrainment and suspension of sediments into a turbulent flow over ripples. J Turbul 4:019
18. Dallali M, Armenio V (2015) Large eddy simulation of two-way coupling sediment transport. Adv Water Resour 81:33–44
19. de Anna P, Le Borgne T, Dentz M, Tartakovsky AM, Bolster D, Davy P (2013) Flow intermittency, dispersion, and correlated continuous time random walks in porous media. Phys Rev Lett 110(18):184502
20. Drake TG, Shreve RL, Dietrich WE, Whiting PJ, Leopold LB (1988) Bedload transport of fine gravel observed by motion-picture photography. J Fluid Mech 192:193–217
21. Einstein HA (1937) The bed load transport as probability problem. Ph.D Thesis. Mitt. der Versuchsanst. Wasserbau Eidg. Technical Hochsch, Zürich
22. Escauriaza C, Sotiropoulos F (2009) Trapping and sedimentation of inertial particles in three-dimensional flows in a cylindrical container with exactly counter-rotating lids. J Fluid Mech 641:169–193
23. Escauriaza C, Sotiropoulos F (2011) Lagrangian model of bed-load transport in turbulent junction flows. J Fluid Mech 666:36–76
24. Frey P, Church M (2009) How river beds move. Science 325(5947):1509–1510
25. Frisch U, Parisi G (1985) On the singularity structure of fully developed turbulence. In: Gil M, Benzi R, Parisi G (eds) Turbulence and predictability in geophysical fluid dynamics. North Holland, New York, pp 84–88
26. Furbish DJ, Schmeeckle MW (2013) A probabilistic derivation of the exponential-like distribution of bed load particle velocities. Water Resour Res 49(3):1537–1551
27. Grass AJ (1971) Structural features of turbulent flows over smooth and rough boundaries. J Fluid Mech 50(02):233–255
28. Harte D (2001) Multifractals: theory and applications. Chapman and Hall/CRC Press, Boca Raton
29. Heathershaw AD, Thorne PD (1985) Sea-bed noises reveal role of turbulent bursting phenomenon in sediment transport by tidal currents. Nature 316(6026):339–342
30. Keshavarzi A, Ball J, Nabav H (2012) Frequency pattern of turbulent flow and sediment entrainment over ripples using image processing. Hydrol Earth Syst Sci 16(1):147–156
31. Keylock CJ, Nishimura K, Peinke J (2012) A classification scheme for turbulence based on the velocity-intermittency structure with an application to near-wall flow and with implications for bed load transport. J Geophys Res 117(F1):F01037
32. Kézdi Á (1974) Handbook of soil mechanics, vol One. Elsevier, Amsterdam

33. Le Moigne A, Qin N (2006) LES with numerical dissipation for aircraft wake vortices. In: 44th AIAA aerospace sciences meeting and exhibit, aerospace sciences meetings
34. Lee H, Ha MY, Balachandar S (2012) Work-based criterion for particle motion and implication for turbulent bed-load transport. Phys Fluids 24(11):116604
35. Link O, González C, Maldonado M, Escauriaza C (2012) Coherent structure dynamics and sediment particle motion around a cylindrical pier in developing scour holes. Acta Geophys 60(6):1689–1719
36. Lu SS, Willmarth WW (1973) Measurements of the structures of the Reynolds stress in a turbulent boundary layer. J Fluid Mech 60:481–571
37. Marion A, Tregnaghi M (2013) A new theoretical framework to model incipient motion of sediment grains and implications for the use of modern experimental techniques. Earth and Planetary Sciences, GeoPlanet, pp 85–100
38. Michaelides EE (2003) Hydrodynamic force and heat/mass transfer from particles, bubbles, and drops. J Fluids Eng 125:209–238
39. Moreno-Casas PA, Bombardelli FA (2015) Computation of the Basset force: recent advances and environmental flow applications. Environ Fluid Mech 16(1):193–208
40. Nelson JM, Shreve RL, McLean SR, Drake TG (1995) Role of near-bed turbulence structure in bed load transport and form mechanics. Water Resour Res 31(8):2071–2086
41. Nikora V, Habersack H, Huber T, McEwan I (2002) On bed particle diffusion in gravel bed flows under weak bed load transport. Water Resour Res 38(6):1081
42. Niño Y, García M (1996) Experiments on particle-turbulence interactions in the near-wall region of an open channel flow: implications for sediment transport. J Fluid Mech 326:285–319
43. Richter DH, Sullivan PP (2013) Momentum transfer in a turbulent, particle-laden Couette flow. Phys Fluids 25:053304
44. Roseberry JC, Schmeeckle MW, Furbish DJ (2012) A probabilistic description of the bed load sediment flux: 2. Particle activity and motions. J Geophys Res 117(F3):F03032
45. Schmeeckle MW (2014) Numerical simulation of turbulence and sediment transport of medium sand. J Geophys Res 119:1240–1262
46. Singh A, Fienberg K, Jerolmack DJ, Marr J, Foufoula-Georgiou E (2009) Experimental evidence for statistical scaling and intermittency in sediment transport rates. J Geophys Res 114(F1):F01025
47. Soldati A, Marchioli C (2012) Sediment transport in steady turbulent boundary layers: potentials, limitations, and perspectives for Lagrangian tracking in DNS and LES. Adv Water Resour 48:18–30
48. Spalding DB (1961) A single formula for the law of the wall. J Apply Mech 28:455–458
49. Sturm TW (2001) Open channel hydraulics (International Edition ed.). McGraw Hill, New York
50. van der Geld CWM (1997) Measurement and prediction of solid sphere trajectories in accelerated gas flow. Int J Multiph Flow 23(2):357–376
51. Vanoni V (1975) Sedimentation engineering In: ASCE task committee for the preparation of the manual on sedimentation of the sedimentation committee of the hydraulics division
52. Vreman AW (2015) Turbulence attenuation in particle-laden flow in smooth and rough channels. J Fluid Mech 773:103–136
53. Vowinckel B, Kempe T, Fröhlich J (2014) Fluid-particle interaction in turbulent open channel flow with fully-resolved mobile beds. Adv Water Resour 72:32–44
54. White FM (1991) Viscous fluid flow, vol 2. McGraw Hill, New York
55. Wu FC, Jiang MR (2007) Numerical investigation of the role of turbulent bursting in sediment entrainment. J Hydraul Eng 133:329–334